https://cimav.repositorioinstitucional.mx/

Enhanced optical properties of $W_{1-x}Mo_xO_3 \cdot 0.33H_2O$ solid solutions with tunable band gaps

A. Arzola-Rubio, J. Camarillo-Cisneros, L. Fuentes-Cobas, V. Collins-Martínez, L. De la Torre-Sáenz, **F. Paraguay-Delgado**

Abstract

A series of $W_{1-x}Mo_xO_3 \cdot 0.33H_2O$ (x = 0, 0.25, 0.50, 0.75) nano/microstructures and $MoO_3 \cdot 0.55H_2O$ with elongated morphology were prepared by using hydrothermal technique. Aqueous acidified solutions of ammonium metatungstate hydrate ($(NH_4)_6H_2W_{12}O_{40} \cdot XH_2O$) and ammonium heptamolybdate tetrahydrate ($(NH_4)_6Mo_7O_{24} \cdot 4H_2O$) were hydrothermally reacted to yield the desired nano/microstructures. In the $WO_3 \cdot 0.33H_2O$ crystal lattice can be substituted with up to 75% Mo without structural alterations. When the Mo atoms increase, from 0 to 75 at. %, the band gap of the, as-prepared, $W_{1-x}Mo_xO_3 \cdot 0.33H_2O$ material decreases from 2.55 to 2.15 eV. In order to corroborate experimental data, first-principle calculations using DFT and DFT + *U* framework were employed which revealed indirect band gap semiconductors up to x = 0.75. We suggest that the increase in the Mo fraction (25%, 50% and 75%) by hydrothermal synthesis (pressure and temperature) is responsible for the narrowing of the band gap.

1. Introduction

Hydrated transition metal oxides such as WO_3nH_2O and MoO_3nH_2O (n = 0, 0.33, 1 or 2) have been studied extensively due to their special electronic and optoelectronic properties. These materials have enormous potential applications in the fields ranging from condensed-matter physics to solid-state chemistry [1], such

https://cimav.repositorioinstitucional.mx/

as photo-electrochemical energy conversion [2], gas sensors [3], photo-catalysts [4], lithium-ion batteries [5], solar cells [6], electron emitters [7] and optical storage media [8]. Hydrated oxides, compared with their single metal oxide constituents (WO_3 and MoO_3), have potential application in electrochemical devices. In the case of solid solutions, molybdenum-tungsten oxide ($W_{1-x}Mo_xO_3 \cdot 0.33H_2O$) materials show more promise due to the ability to control the components, structural characteristics tailoring, physical/chemical properties modulation. Furthermore, an improvement in the performance in the above-mentioned applications is expected due to the "synergistic effect" in the composites, when Mo is included in the lattice. Recently, tremendous effort has been dedicated to the preparation [9]; [10] ; [11], formation, mechanism study [12]; [13] ; [14], and property investigation of $W_{1-x}Mo_xO_3 \cdot 3H_2O$. The $W_{1-x}Mo_xO_3 \cdot 3H_2O$ showed improved electrochromic [15]; [16]; [17] ; [18], gas sensing [19]; [20]; [21]; [22] ; [23], catalytic [24], lithium ion transport [25], and photocatalytic properties [26] when it is compared with their unary oxide counterparts WO_3 or MoO_3. Recently, Zhou et al. was capable of modulating the band gaps of the $W_{1-x}Mo_xO_3 \cdot 3H_2O$ materials by changing the Mo/W ratio [30]. They successfully prepared a series of $W_{1-x}Mo_xO_3$–$0.33H_2O$ micro/nanostructures with controlled stoichiometry (x = 0, 0.25, 0.50, 0.75). Additionally, they revealed that when the Mo content is increased, the band gap of $W_{1-x}Mo_xO_3$–$0.33H_2O$ narrowed from 3.25 to 2.77 eV. They finally concluded that the energy level of the M5+ fraction which enhanced the intervalency-transition is responsible for the narrowing of the band gap.

https://cimav.repositorioinstitucional.mx/

In this work, we synthesized a series of $W_{1-x}Mo_xO_3$–$0.33H_2O$ nano/microstructures similar to those of Zhou et al. using different precursors such as ammonium heptamolybdate and ammonium metatungstate, instead of pure metal powders. $HNO_3$was used to acidify the solutions instead of forming the peroxo-polytungstic and molybdic acid solutions. The enhanced band gaps were evaluated as a function of the Mo quantity contents.

2. Synthesis and characterization

2.1. Chemicals

Ammonium metatungstate hydrate ($(NH_4)_6H_2W_{12}O_{40}\cdot xH_2O$), ammonium heptamolybdate tetrahydrate ($(NH_4)_6Mo_7O_{24}\cdot 4H_2O$), Hydrogen peroxide ($H_2O_2$, 30 wt.%), and Nitric acid (HNO_3, 70 wt.%) were purchased from Sigma–Aldrich.

2.2. Synthesis

The initial solutions "*y*" mmol (*y* = 0, 2.5, 5.0, 7.5, and 10.0 of Ammonium heptamolybdate tetrahydrate and (10-*y*) mmol of Ammonium metatungstate hydrate) were dissolved in a mixture of 21 mL of tridistilled H_2O, 9 mL of 30 wt.% H_2O_2, and 3 mL of 2.2 M HNO_3. Each solution was then transferred into a Teflon vial and placed in a stainless-steel autoclave, sealed and hydrothermally treated at 180 °C for 24 h. The solid solutions were collected via centrifugation, then were washed with tridistilled water 3 times, and finally dried at room temperature. The resultant products with *y* = 0, 2.5, 5.0, 7.5, and 10.0 are designated as $WO_3\cdot 0.33H_2O$ (WH1), $W_{0.75}Mo_{0.25}O_3\cdot 0.33H_2O$ (WM25), $W_{0.50}Mo_{0.50}O_3\cdot 0.33H_2O$ (WM50), to $W_{0.25}Mo_{0.75}O_3\cdot 0.33H_2O$ (WM75), and to $MoO_3\cdot 0.55H_2O$ (MH1), for simplification the names in the rest of text.

https://cimav.repositorioinstitucional.mx/

2.3. Characterization

X-ray diffraction (XRD) patterns were obtained by conventional diffractometry and by means of synchrotron radiation. Conventional diffraction was recorded on a Philips X'Pert MPD X-ray Diffractometer with Cu Kα1 radiation (λ = 1.54056 Å) at 40 kV and a current of 30 mA. Synchrotron data was collected at the MCX beamline of Elettra synchrotron in Trieste. Symmetric reflection (Bragg–Brentano) geometry was employed to acquire data. The selected wavelength is λ = 0.9500 Å which was confirmed by measurement of a silicon standard and led to the determination of the instrumental resolution function. The measurement angular domain was $10° < 2\theta < 60°$, step $\lambda(2\theta) = 0.01°$. Experimental versus theoretical fitting was realized employing the Rietveld method up to the weighted profile *R*-factor (R_{wp}) minimum of 16% as implemented in Reflex software package, lattice parameters are reported after fitting process, and these parameters were used for ab initio calculations using the Quantum Espresso code. Scanning electron microscopy (SEM) images were obtained on a cold field emission JEOL JSM-7401F microscope operated at 5 and 17 kV. An energy-dispersive X-ray spectroscopy (EDS) facility (Oxford INCA X-Sight) attached to the SEM was employed to analyze the chemical composition. Transmission electron microscope (TEM) experiments were conducted on field emission JEOL JEM-2200FS microscope with an accelerating voltage at 200 kV. The samples for TEM study were dispersed in methanol by sonication and then deposited onto a lacy carbon film on a copper grid. UV–Vis diffusive reflectance spectra (DRS) were obtained on a Lambda 9 UV–Vis spectrometer. The Brunauer–Emmett–Teller (BET) surface areas were measured on a nitrogen adsorption equipment (Quadrasorb SI, Quantachrome), the samples were degassed at 150–

https://cimav.repositorioinstitucional.mx/

250 °C for 12 h before the measurement. Raman spectroscopy was done using Micro RAMAN Labram VIS-63 operated at room temperature; with a 632.8 nm wavelength standard He–Ne laser. All ab initio calculations were performed using the Quantum Espresso code in the frame-work of density functional theory (DFT). Due to the known band gap sub estimation in DFT treatments [31] ; [32] (by the presence of “d” orbitals in W and Mo atoms) DFT + *U* method was employed. The models for calculating WH1 and MH1 oxides were to reduce the unit cells from conventional to primitive, while in the case of solid solutions (WM25, WM50 and WM75) were calculated by means of 2 × 2 × 1 supercells. In all systems, the hydrated unit cell were employed (to XRD pattern fitting and to DFT calculations), however in both theoretical approach the presence of H atoms were excluded.

3. Experimental results

In the synthesis process, the mixture of ammonium metatungstate hydrate ($(NH_4)_6H_2W_{12}O_{40}\cdot XH_2O$) and ammonium heptamolybdate tetrahydrate ($(NH_4)_6Mo_7O_{24}\cdot 4H_2O$) solutions was prepared by dissolving these salts in tridistilled H_2O, H_2O_2, and 2.2 M HNO_3. In the case of pure ammonium metatungstate hydrate it is a clear solution but, when Mo salt is added, the color of the solution changes from clear to bright yellow as the Mo content increases, the solution keeps the same bright yellow. The hydrothermal synthesis at 180 °C accomplished the crystallization of $W_{1-x}Mo_xO_3\cdot 0.33H_2O$ from ammonium metatungstate hydrate ($(NH_4)_6H_2W_{12}O_{40}\cdot XH_2O$) and ammonium heptamolybdate tetrahydrate ($(NH_4)_6Mo_7O_{24}\cdot 4H_2O$) solutions at high vapor pressures. The XRD patterns as a function of Mo content are shown in Fig. 1. For WH1, the indexing corresponds to

https://cimav.repositorioinstitucional.mx/

Orthorhombic crystal, with space group Aba2 and lattice parameters a = 7.323 Å, b = 7.690 Å, c = 12.772 Å (taken from ICSD using POWD-12++ 228, 695 (1997)). For patterns which there are Mo atom content at (x = 0:25; 0:50, and 0:75), the crystal structure and space group were maintained, indicating that W atoms can be substituted in $WO_3 \cdot 0.33H_2O$ with up to 75% Mo atoms.

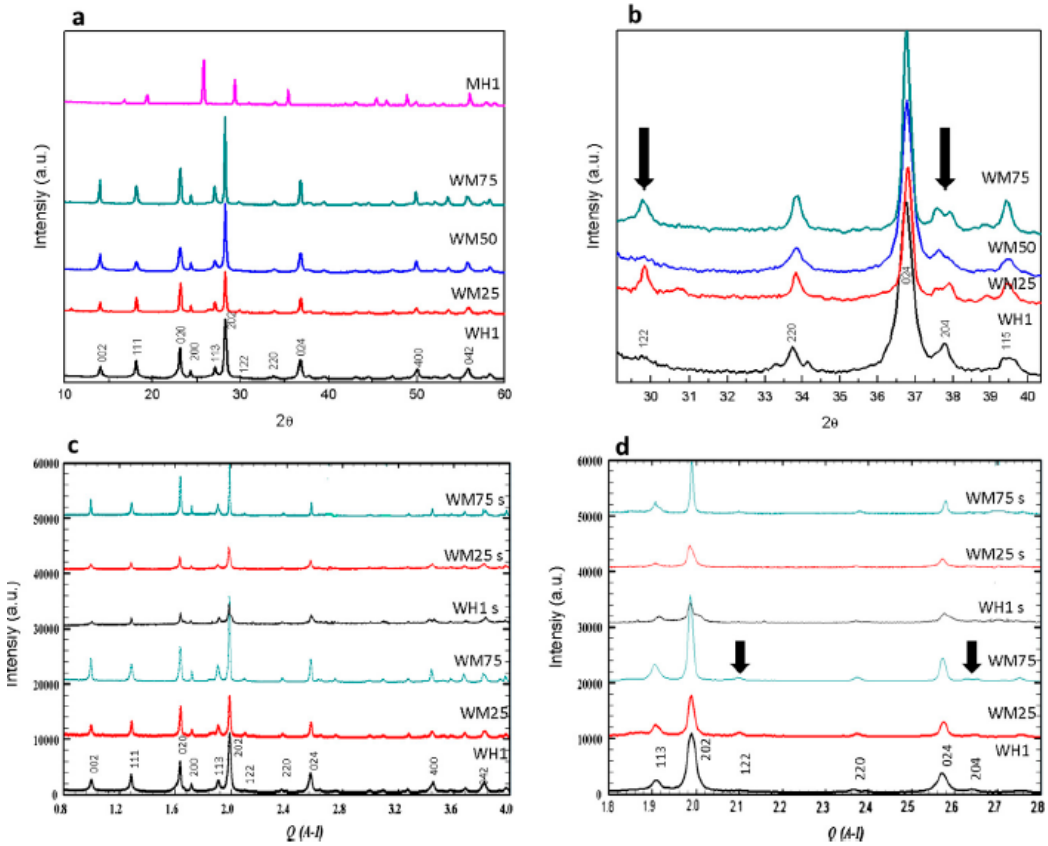

Fig. 1. XRD patterns from (a) conventional and (b) higher resolution by synchrotron, (c) and (d) zoom showing the little changes.

However, slight modifications were observed. New diffraction peaks appear when the Mo content increases. These changes are located at 2θ = 29.8 and 2θ = 37.74 (detailed changes are in Fig. 1b and d marked by arrows). In all samples,

https://cimav.repositorioinstitucional.mx/

the peak located at 37.74 starts splitting progressively into two peaks. According to [9] ; [33] the appearance of new diffraction peaks, in this case, is due to the reduced symmetry from an F-centered orthorhombic cell for $WO_3 \cdot 0.33H_2O$ to a C-centered orthorhombic cell for $W_{0.25}Mo_{0.75}O_3 \cdot 0.33H_2O$ caused by increased distortions induced by Mo substitution. The new diffraction and splitting peaks can be seen clearly in Fig. 1b. For the case of MH1 (x = 1.00), the XRD pattern can be assigned to a hexagonal $MoO_3 \cdot 0.55H_2O$ (Index by ICSD using POWD-12++ 228, 695 (1997), space group P63/m with lattice parameters a = 1.0584 nm, b = 1.0584 nm, c = 0.3727 nm).

Three samples (WH1, WM25 and WM75) were taken at the Elettra Synchrotron at Trieste for a more precise and higher resolution XRD pattern due a shorter wavelength the synchrotron produces compared to conventional sources (1.54 Å vs 0.95 Å), as well as better monochromaticity. The XRD pattern comparison between conventional and Synchrotron can be observed in Fig. 1c. In this case, the patterns depict Intensity vs. Q ($Å^{-1}$), the Q values are calculated by the equation $Q = 4\pi \sin \Theta/\lambda$. From these patterns, the three at the bottom of Fig. 1c corresponds to WH1, WM25 and WM75 made in a conventional XRD and the three XRD patterns on top belong to the same samples. The patterns acquired by synchrotron do not show major changes or shift of peaks but confirm the structure and purity of samples.

The BET surface areas of the products have been measured by N_2 adsorption in the relative pressure range from 0.05 to 0.3 p/p_0. There are two major factors that influence the BET surface areas of the products, the particle size and the Mo

https://cimav.repositorioinstitucional.mx/

content. WH1 compound shows the largest BET surface area of 68.5 m^2/g due to the high W content. For the Mo solid solution materials ($W_{1-x}Mo_xO_3 \cdot 0.33H_2O$), the particle size plays a more important role. When the Mo atom content increases from 0 to 0.75, the surface area of the products decreases from 68.5 to 15 m^2/g, which can be attributed to the increase of the primary particle size deduced from the sharpening of the diffraction peaks shown in the XRD patterns and images.

Fig 2 represents the SEM images from all materials synthesized. The secondary images for WH1 (2a), WM25 (2b), WM50 (2c) and WM75 (2d), are generally flake-like, with different size in diameter below 200 nm and thickness around 20 nm. Fig. 2b shows elongated rods with small flakes around it. The morphology changes for sample MH1, the image shows hexagonal elongated micro-irregular particles with a width and length of approximately 7000 and 75,000 nm, respectively. The summary of measurements and morphology types are shown at Table 1.

https://cimav.repositorioinstitucional.mx/

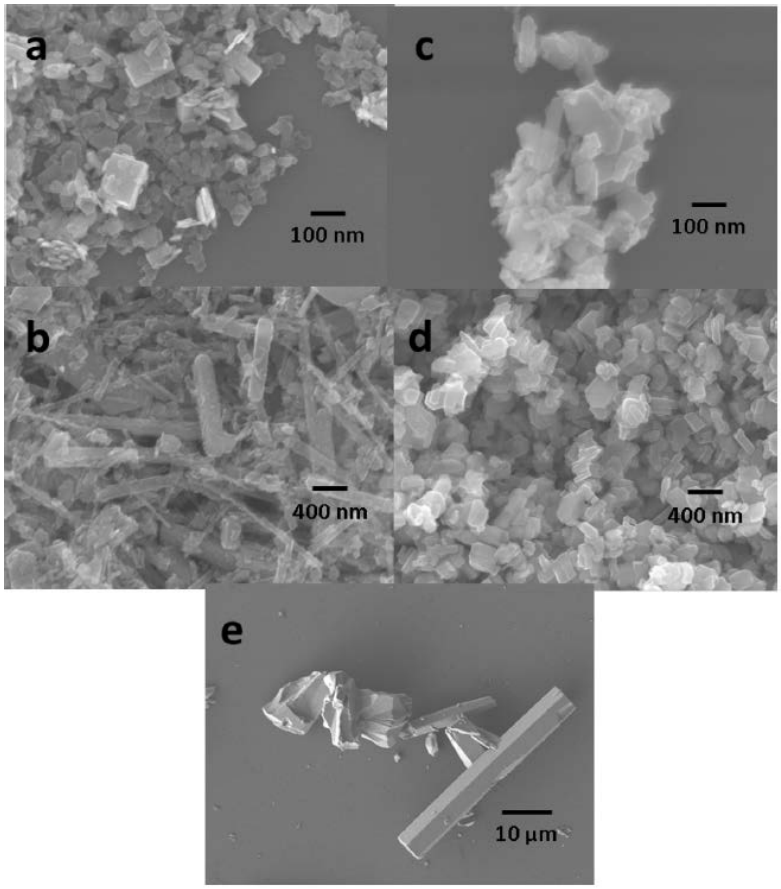

Fig. 2. SEM images of (a) WH1, (b) WM25, (c) WM50, (d) WM75, and (e) MH1.

Table 1
Theoretical and experimental Mo content, BET surface area, and band gap and particle size.

Sample	$X_{Theoritical}$ [1]	X_{EDS} [2]	S_{BET} (m^2/g) [3]	E_g (eV) [4]	E_g (eV) [5]	E_g (eV) [6]	Particle size (nm)	Particle shape (like)
WH1	0	0	68.5	2.55	0.491	2.63	73 ± 35	Flakes
WM25	25	21	46.0	2.37	0.435	2.26	337 ± 223	Flakes and needles
WM50	50	37	40.1	2.35	0.433	2.04	103 ± 65	Flakes
WM75	75	55	15.0	2.15	0.418	1.98	163 ± 57	Flakes
MH1	100	100	1.0	2.25	–	–	4500 ± 15,000	Hexagonal elongated

[1] Theoretical Mo content.
[2] Mo content determined from EDS.
[3] BET surface area.
[4] Band gap (optical).
[5] DFT band gap.
[6] DFT + U band gap.

https://cimav.repositorioinstitucional.mx/

Fig. 3 shows bright field transmission electron micrographs for all studied materials. The first four images show “hexagonal” flake-like morphologies with a length and width of around 600 nm and 150 nm, respectively. For sample MH1, we observe micrometric size particles with an irregular hexagonal rod shape. For each image, the selected area electron diffraction (SAED) zones are marked with a circle, for all solid solutions from the compounds described above. All diffraction patterns show the presence of monocrystalline particles. The set of diffraction spots (Fig. 3b) can be indexed as the [−4, 2, −1] zone axis of monocrystalline orthorhombic $WO_3 \cdot 0.33H_2O$. Fig. 3d the [3, 0, −1] zone axis corresponds to orthorhombic structure $W_{75}Mo_{25}O_3 \cdot 0.33H_2O$. The [2, −1, 0] zone axis can be indexed to material $W_{50}Mo_{50}O_3 \cdot 0.33H_2O$ (Fig. 3f). For Fig. 3h, we have the zone axis [−2, −1, 2] which corresponds to the crystal $W_{25}Mo_{75}O_3 \cdot 0.33H_2O$. In the case of MH1, the diffraction pattern was indexed with [−3, 1, −3] zone axis at Fig. 3j.

https://cimav.repositorioinstitucional.mx/

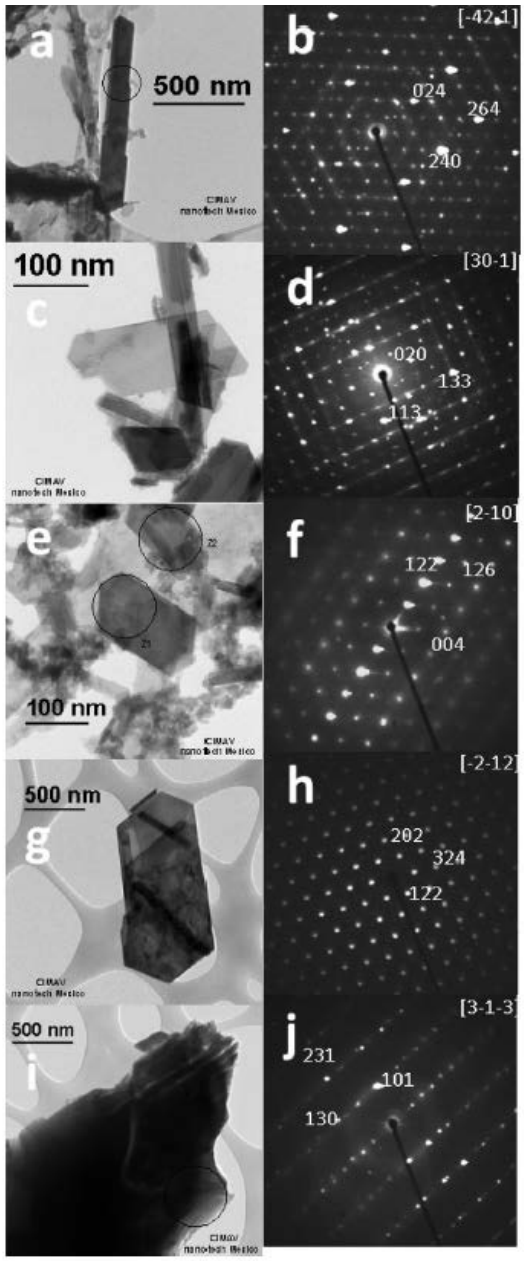

Fig. 3. TEM images (b, d, f, h, j), and ED patterns (a, c, e, g, i) of WH1, WM25, WM50, WM75 and MH1.

The optical properties of the samples were studied from their respective diffuse reflectance spectra, the results are shown in Fig. 4a. The absorption zone for each solid solution material systematically shifts with respect to the Mo atoms

https://cimav.repositorioinstitucional.mx/

content. The shifts are from the UV to the visible light spectral region and can be attributed to the Mo substitution of W. The effective reduction in the band gap (BG) of these solid solutions was then ascertained due to the incorporation of Mo. Fig. 4b shows the band gap determination for all samples, for this purpose $[F(R)hv]^n$ was plotted against hv. Since these $W_{1-x}Mo_xO_3 \cdot 0.33H_2O$ materials are indirect band gap semiconductors, the value of $n = 1/2$ ($n = 2$ for direct band gap) [29]. The linear part of $[F(R)hv]^{1/2}$ vs. hv curve at $[F(R)hv]^{1/2} = 0$ represents the band gap. Along with the Mo atom increase, the oxygen defect band states are also formed in the band gap. In the case of pure WO_3, the electronic transition occurs directly from the upper part of the valence band (VB) to the lowest part of the conduction band (CB). The values are rather similar to that of $WO_3 \cdot 0.33H_2O$, but in the case of different Mo/W rate content samples, show more reflectance in the visible range (~440 nm). After a 25% Mo substitution, a significant shift was notice, when compared to $WO_3 \cdot 0.33H_2O$, indicating a narrowing of the band gap. This shift occurs in direct correlation with the increase in Mo substitution. The band gaps of the solid solutions materials for $x = 0.25$, 0.50, and 0.75, are 2.37, 2.35, and 2.15 eV, respectively. The band gap of MH1, which is 2.25 eV, does not follow the trend of the $W_{1-x}Mo_xO_3 \cdot 0.33H_2O$ solid solutions due to the structural difference caused by molybdenum oxide.

https://cimav.repositorioinstitucional.mx/

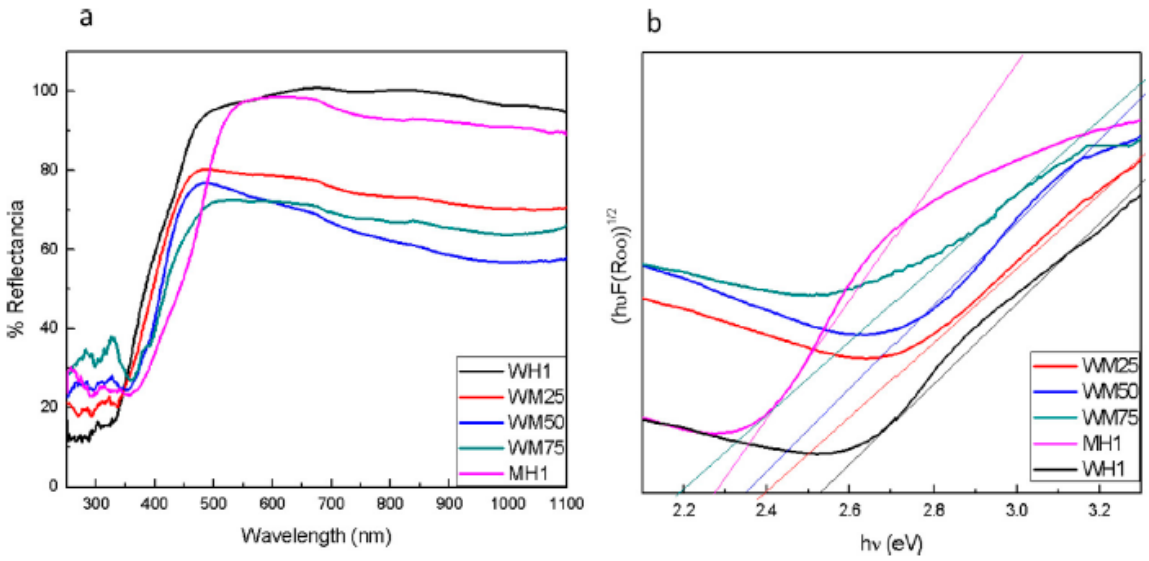

Fig. 4. Diffuse reflectance, Kubelka–Munk curves, and band gap determination. (a) Diffuse reflectance (% R) spectra of solid solutions (b) determination of band gap of each sample by drawing a line at [F(R)hm]1/2 = 0.

Diffuse reflection spectra (DRS) clearly demonstrates the importance of structure (crystalline phase) when studying the composition-property relationship of the binary $W_{1-x}Mo_xO_3$ materials and the subsequent changing in the band gap values. Therefore, this shows that band gap can be tuned for specific applications by changing the Mo content of the material.

The band gap determination by simulation methodology using DFT results in a systematic decrease in the values for electronic band gap in direct correlation with Mo substitution, decreasing from 0.491 eV for WH1, to 0.435, 0.433 and 0.418 eV, for WM25, WM50 and WM75, respectively. However, a metallic character was calculated for MH1, which disagrees with the measured experimental value. The band gap trend was also investigated by incorporating the Hubbard correction, to determine the on-site Coulomb potential for the WH1 system [36]. For this purpose, the *U* values were varied from 1 to 10 eV, relaxing in every case, and the *U* = 9 eV

https://cimav.repositorioinstitucional.mx/

value was able to reproduce the experimental results. This *U* value was applied to all other Mo atoms solution materials in order to take an approach that is independent of the amount of added Mo. This potential was applied over the “d” orbital of the oxygen atoms. The band gap structure and density of states showed in Fig. 5 corresponds to the results of DFT + *U* calculations, which had the same band gap trend (i.e. the band gap decrease as a function of the Mo amount), obtaining 2.63 eV for WH1, 2.26 eV for WM25, 2.04 eV for WM50 and 1.98 eV for WM75, all of which are considering an indirect transition. The employed models are independent of Mo atomic positions; this was concluded after several tested configurations on every composition, without significant differences in the band gap values. The gap reduction due to the addition of Mo is in direct consequence to the presence of extra bands below the conduction bands. Here, we are presenting just the qualitative result. Our model correctly captures the current trend from WH1 to WM75; however, the rate of change depending on the amount of added Mo is higher than the experimental values. Furthermore, in accordance with DFT calculations, it was not possible to obtain any semiconductor character in the MH1 structure. The clear relationship between band structures of the hydrated compound MH1 and its anhydrate analogy α-MoO_3[37], which presents electronic gap, suggests that the measured gap could result from the combined presence of molybdenum oxide created by O vacancies. Different MH1 models with O vacancies were tested, despite the metallic character they was not modified. In our employed models, it was not possible to investigate the importance of taking into account H atoms (thus dispersive forces) and its effect on the electronic gap. The comparative values about

https://cimav.repositorioinstitucional.mx/

band gap are shown in the Table 1.

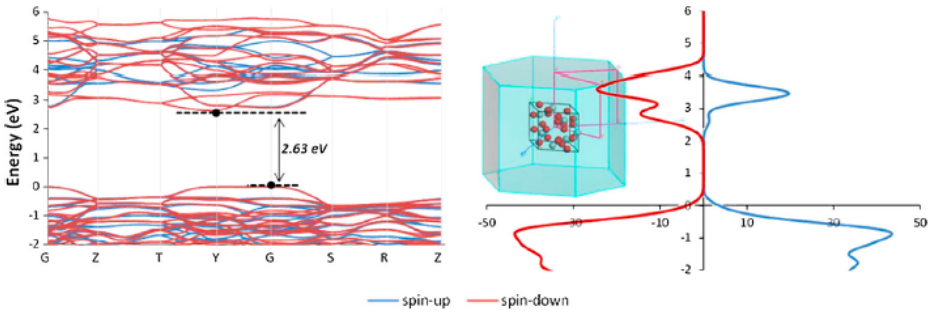

Fig. 5. (a) Band structures and (b) density of states; both plots correspond to WH1 compound obtained from the unit cell (and Brillouin zone) contained like inset in (b). The U value corresponds to 9 eV.

In the Raman spectra, Fig. 6 reveal that all compounds (sample patterns were normalized), except MH1, show two strong peaks at 720 and 813 cm^{-1}, one medium peak at 280 cm^{-1} and one weak peak located at 336 cm^{-1}. There are very weak signals at 450 and 1000 cm^{-1}, respectively. The two strong peaks located at 720 and 813 $cm^{-1}$are due to stretching vibrations v(W—O—W) of the bridging oxygen atoms, the peak at 336 cm^{-1} is characteristic of ς(O—W—O) deformation mode, and the weak signal at 1025 cm^{-1} could be attributed to the stretching mode of the terminal W═O double bond [34]. Because the solid solutions containing X = 0.25, 0.50, and 0.75 (WM25, WM50 and WM75) are quite similar to the X = 0 (WH1), the Raman spectra show structural similarity of these samples.

https://cimav.repositorioinstitucional.mx/

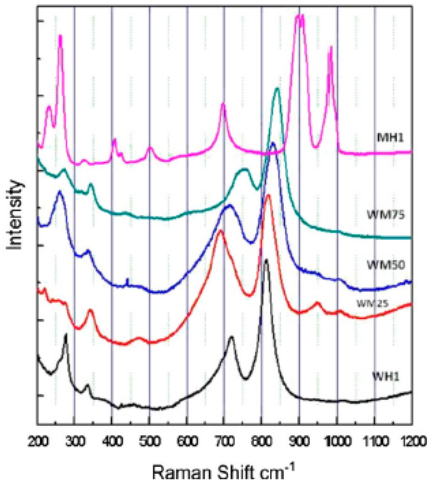

Fig. 6. Raman shifts of WH1, WM25, WM50, WM75 and MH1.

When the Mo atoms are in the crystal cell, there is a shift in the position of some bands. The bands located at 720 and 813 cm^{-1} gradually shift to 750 and 845 cm^{-1}, respectively, for the WM75 sample. At the same time these peaks become broader, which may be due to either disorder or loss of long distance translational periodicity (of high atomic number atoms) [35]. For MH1, the representative Raman bands of $MoO_3 \cdot 0.55H_2O$ are the frequency range of 200–1000 cm^{-1}. At 900 and 1000 cm^{-1}, we observe two bands that correspond to v(O═Mo═O) and v(Mo═O) stretching, respectively. The band located at 700 cm^{-1} can be attributed to v(OMo_2) and v(OMo_3) stretching. The bands located at 400 and 500 cm^{-1} can be assigned to deformation modes. In the case of the band located at 340 cm^{-1}, it corresponds to a v(Mo—OH_2) stretching. Below 300 cm^{-1}, we observe bands that are due to deformation and lattice modes. All assignments can be found in Table 2.

https://cimav.repositorioinstitucional.mx/

Table 2
Raman frequencies (cm^{-1}) of $W_{1-x}Mo_xO_3 \cdot 0.33H_2O$ and $MoO_3 0{:}55H_2O$ at ambient conditions.

WH1, WM25, WM50 and WM75 (cm^{-1})	$MoO_3 0{:}55H_2O$ (cm^{-1})	Assignment
	1000–900	ν(Mo═O) stretching
		ν(O═Mo═O) stretching
1000		W═O stretching
800–700		ν(W—O—W) stretching
	700	ν(OMo_2) stretching
		ν(OMo_3) stretching
	500–400	Deformation modes
350		ς(O—W—O) deformation
	340	ν(Mo—OH_2) stretching
	<300	Deformation modes

4. Conclusion

A series of Mo atoms solid solution ($W_{1-x}Mo_xO_3 \cdot 0.33H_2O$) with controlled stoichiometry (x = 0, 0.25, 0.50, 0.75) from a salt precursor were synthesized. The lattice of ($WO_3 \cdot 0.33H_2O$) can be substituted with up to 75% Mo without structural alteration. As the Mo content increases, the band gap of the materials narrowed from 2.55 to 2.15 eV. This result can be applied for use this materials on the visible light absorption for photocatalysis, photovoltaics, and hydrogen generation. DFT + U calculations showed that gap narrow was due to added bands below conductions level of the original $WO_3 \cdot 0.33H_2O$ compound. We think that the properties of these enhanced compounds make them suitable for applications in the visible light spectra.

Acknowledgments

The authors are thankful to the Centro Nacional de Supercomputo (CNS) of Instituto Potosino de Investigación Científica y Tecnologicá (IPICyT) for computational resources, with CIMAV-NANOTECH and Rodrigo Domínguez for provided support. JCC is supported by CONACYT – México scholarships 290674

https://cimav.repositorioinstitucional.mx/

and 290604. Thanks to the CEMISOL-SENER-Conacyt project 207450/No P31. Thanks to C. Ornelas, W. Antunez and P. Piza for technical help at the Nanotech lab. And finally thanks to the Electra Synchrotron for the facility at beam line MCX.

Reference

[1] H. Zheng, J.Z. Ou, M.S. Strano, R.B. Kaner, A. Mitchell, K. Kalantar-zadeh, Adv. Funct. Mater. 21 (2011) 2175 (ISSN 1616-3028).

[2] S. Higashimoto, N. Kitahata, K. Mori, M. Azuma, Catal. Lett. 101 (2005) 49 (ISSN 1011–372X).

[3] Y.S. Kim, S.-C. Ha, K. Kim, H. Yang, S.-Y. Choi, Y.T. Kim, J.T. Park, C.H. Lee, J. Choi, J. Paek, K. Lee, Appl. Phys. Lett. 86 (2005) 213105.

[4] C. Yu, J. Yu, W. Zhou, K. Yang, Catal. Lett. 140 (2010) 172.

[5] N.A. Galiote, F. Huguenin, J. Phys. Chem. C 111 (2007) 14911.

[6] H. Zheng, Y. Tachibana, K. Kalantar-zadeh, Langmuir 26 (2010) 19148.

[7] X. Zhang, L. Gong, K. Liu, Y. Cao, X. Xiao, W. Sun, X. Hu, Y. Gao, J. Chen, J. Zhou, Z.L. Wang, Adv. Mater. 22 (2010) 5292 (ISSN 1521-4095).

[8] I. Turyan, U.O. Krasovec, B. Orel, T. Saraidorov, R. Reisfeld, D. Mandler, Adv. Mater. 12 (2000) 330 (ISSN 1521-4095).

[9] F. Harb, B. Gerand, M. Figlarz, C.R. Acad. Sci. Paris 303 (1986) 789.

[10] F. Harb, B. Gerand, M. Figlarz, C.R. Acad. Sci. Paris 303 (1986) 445.

[11] M. Figlarz, Prog. Solid State Chem. 19 (1989) 1.

[12] R. Kiebach, N. Pienack, W. Bensch, J.D. Grunwaldt, A. Michailovski, A. Baiker, T. Fox, Y. Zhou, G.R. Patzke, Chem. Mater. 20 (2008) 3022.

https://cimav.repositorioinstitucional.mx/

[13] A. Michailovski, F. Krumeich, G.R. Patzke, Chem. Mater. 16 (2004) 1433.

[14] Y. Zhou, N. Pienack, W. Bensch, G.R. Patzke, Small 5 (2009) 1978.

[15] B.W. Faughnan, R.S. Crandall, Appl. Phys. Lett. 31 (1977) 834.

[16] K.A. Gesheva, T. Ivanova, Chem. Vap. Deposition 12 (2006) 231.

[17] T. Ivanova, K.A. Gesheva, A. Szekeres, J. Solid State Electrochem. 7 (2002) 21.

[18] B. Xue, J. Peng, Z.F. Xin, Y.M. Kong, L. Li, B. Li, J. Mater. Chem. 15 (2005) 4793.

[19] K. Galatsis, YX. Li, W. Wlodarski, C. Cantalini, M. Passacantando, J. Sol–Gel Sci. Technol. 26 (2002) 1097.

[20] K. Galatsis, YX. Li, W. Wlodarski, E. Comini, Sens. Actuators, B 83 (2002) 276.

[21] K. Galatsis, YX. Li, W. Wlodarski, K. Kalantar-zadeh, Sens. Actuators B 77 (2001) 478.

[22] C. Malagu, M.C. Carotta, A. Cervi, V. Guidi, G. Martinelli, J. Appl. Phys. 101 (2007) 104310.

[23] O. Merdrignac-Conanec, P.T. Moseley, J. Mater. Chem. 12 (2002) 1779.

[24] H. Nair, M.J. Liszka, J.E. Gatt, C.D. Baertsch, J. Phys. Chem. C 112 (2008) 1612.

[25] L. Kondrachova, B.P. Hahn, G. Vijayaraghavan, R.D. Williams, K.J. Stevenson, Langmuir 22 (2006) 10490.

https://cimav.repositorioinstitucional.mx/

[26] S.H. Baeck, T.F. Jaramillo, D.H. Jeong, E.W. McFarland, Chem. Commun. 390 (2004).

[27] A. Taurino, M. Catalano, R. Rella, P. Siciliano, W. Wlodarski, J. Appl. Phys. 93 (2003) 3816.

[28] R.A. May, L. Kondrachova, B.P. Hahn, K.J. Stevenson, J. Phys. Chem. C 111 (2007) 18251.

[29] S. Morandi, M.C. Paganini, E. Giamello, M. Bini, D. Capsoni, V. Massarotti, G. Ghiotti, J. Solid State Chem. 182 (2009) 3342.

[30] L. Zhou, J. Zhu, M. Yu, X. Huang, Z. Li, Y. Wang, C. Yu, J. Phys. Chem. C 114 (2010) 20947.

[31] J. Ruiz-Fuertes, S. Lopez´-Moreno, J. Lopez-Solano, D. Errandonea, A. Segura, R. Lacomba-Perales, A. Munoz, S. Radescu, P. Rodriguez-Hernandez, M. Gospodinov, L. Nagornaya, C. Tu, Phys. Rev. B 86 (September) (2012) 125202. <http://link.aps. org/doi/10.1103/PhysRevB.86.125202>.

[32] V. Panchal, D. Errandonea, A. Segura, P. Rodriguez-Hernandez, A. Muñoz, S. Lopez-Moreno, M. Bettinelli, J. Appl. Phys. 110 (2011).

[33] F. Hard, B. Gérand, G. Nowogrocki, M. Figlarz, Solid State Ionics 32–3 (1989) 84.

[34] M.F. Daniel, B. Desbat, J.C. Lassegues, B. Gerand, M. Figlarz, J. Solid State Chem. 67 (1987) 235–247.

[35] Ph. Colomban, Stress- and nanostructure-imaging of ceramic fibers and abradable thermal barrier coatings by Raman microspectrometry: state of the art and perspectives, Ceram. Eng. Sci. Proc. 21 (2000) 143.

https://cimav.repositorioinstitucional.mx/

[36] A.I. Liechtenstein, V.I. Anisimov, J. Zaane, Phys. Rev. B 52 (1995) R5467.

[37] Y. Lei, Z. Chen, J. Phys. Chem. C 116 (2012) 25757–25764.